Article

Terrestrial photosynthesis inferred from plant carbonyl sulfide uptake

https://doi.org/10.1038/s41586-024-08050-3

Received: 22 August 2023

Accepted: 13 September 2024

Published online: 16 October 2024

Check for updates

Jiameng Lai[1], Linda M. J. Kooijmans[2], Wu Sun[3], Danica Lombardozzi[4], J. Elliott Campbell[5], Lianhong Gu[6], Yiqi Luo[1], Le Kuai[7] & Ying Sun[1]✉

Terrestrial photosynthesis, or gross primary production (GPP), is the largest carbon flux in the biosphere, but its global magnitude and spatiotemporal dynamics remain uncertain[1]. The global annual mean GPP is historically thought to be around 120 PgC yr^{-1} (refs. 2–6), which is about 30–50 PgC yr^{-1} lower than GPP inferred from the oxygen-18 (^{18}O) isotope[7] and soil respiration[8]. This disparity is a source of uncertainty in predicting climate–carbon cycle feedbacks[9,10]. Here we infer GPP from carbonyl sulfide, an innovative tracer for CO_2 diffusion from ambient air to leaf chloroplasts through stomata and mesophyll layers. We demonstrate that explicitly representing mesophyll diffusion is important for accurately quantifying the spatiotemporal dynamics of carbonyl sulfide uptake by plants. From the estimate of carbonyl sulfide uptake by plants, we infer a global contemporary GPP of 157 (±8.5) PgC yr^{-1}, which is consistent with estimates from ^{18}O (150–175 PgC yr^{-1}) and soil respiration (149^{+29}_{-23} PgC yr^{-1}), but with an improved confidence level. Our global GPP is higher than satellite optical observation-driven estimates (120–140 PgC yr^{-1}) that are used for Earth system model benchmarking. This difference predominantly occurs in the pan-tropical rainforests and is corroborated by ground measurements[11], suggesting a more productive tropics than satellite-based GPP products indicated. As GPP is a primary determinant of terrestrial carbon sinks and may shape climate trajectories[9,10], our findings lay a physiological foundation on which the understanding and prediction of carbon–climate feedbacks can be advanced.

Terrestrial ecosystems remove carbon dioxide (CO_2) from the atmosphere through photosynthesis, which is the largest carbon flux on Earth and fuels subsequent processes of the terrestrial carbon cycle[12]. Despite decades of effort to quantify photosynthetic CO_2 uptake (or GPP), substantial uncertainty remains in its global magnitude, spatial patterns, temporal dynamics and environmental responses[6,8,13,14]. This uncertainty cascades into predicting carbon–climate feedbacks[1]. The global GPP has been estimated to be around 120 PgC yr^{-1} since the early 1980s[2,3], a value that has later been reiterated by remote sensing[4,5]. However, this value is at odds with independent inferences based on the ^{18}O signature of atmospheric CO_2 (150–175 PgC yr^{-1})[7] and soil respiration (149^{+29}_{-23} PgC yr^{-1})[8]. Such uncertainties present challenges for projecting the future trajectories of terrestrial carbon sinks[15] and call for new constraints on GPP and its spatiotemporal patterns[1].

Carbonyl sulfide (OCS or COS) is a trace gas in the atmosphere, whose concentration is six orders of magnitude lower than that of CO_2 (ref. 16). Plants take up OCS through a diffusion pathway shared with CO_2 and consume it by carbonic anhydrase (CA) within leaves. As the hydrolysis of OCS by CA is irreversible, plant OCS uptake, unlike CO_2 exchange, is not offset by any production process and thereby tracks GPP. Moreover, the plant uptake, the dominant sink of atmospheric OCS, is spatially separated from its main sources (that is, ocean and industrial sources)[17]. Consequently, the continental-scale uptake of OCS and CO_2 (that is, GPP) are coupled[10,17].

Quantifying GPP from OCS fluxes requires a realistic representation of OCS diffusion (from ambient air to leaf chloroplasts) and reaction processes (consumption by CA) along the soil–plant–atmosphere continuum[16], as implemented in terrestrial biosphere models (TBMs). The OCS consumption through CA (g_{CA}^{OCS}) is generally not considered a limiting factor for OCS exchange[18]. OCS diffusion parallels CO_2 diffusion, as they share the pathway from ambient air through the leaf boundary layer, stomata, mesophyll layers and to their respective reactive sites[16]. Along this pathway, the boundary layer conductance g_b and stomatal conductance g_s for CO_2 ($g_b^{CO_2}$ and $g_s^{CO_2}$, respectively) have been represented in most TBMs[19]. Such formulations can be adapted to represent the counterparts for OCS (that is, g_b^{OCS} and g_s^{OCS}), after accounting for the different molecular diffusivities of OCS and CO_2 in air[16]. However, the mesophyll conductance (g_{mes}) has long been neglected in TBMs, even though mesophyll layers act as a major barrier (with a magnitude comparable to g_s) to the movement of both CO_2 and OCS inside leaves of C_3 plants[20,21]. Here g_{mes}^{OCS} is assumed to be equal to $g_{mes}^{CO_2}$, as the aqueous diffusivities of CO_2 and OCS are similar[22,23]. Unless otherwise specified, we use g_{mes} to denote mesophyll conductance for both CO_2 and OCS.

[1]School of Integrative Plant Science, Cornell University, Ithaca, NY, USA. [2]Meteorology and Air Quality, Wageningen University and Research, Wageningen, The Netherlands. [3]Department of Global Ecology, Carnegie Institution for Science, Stanford, CA, USA. [4]Colorado State University, Fort Collins, CO, USA. [5]University of California, Santa Cruz, Santa Cruz, CA, USA. [6]Environmental Sciences Division and Climate Change Science Institute, Oak Ridge National Laboratory, Oak Ridge, TN, USA. [7]Jet Propulsion Laboratory, California Institute of Technology, Pasadena, CA, USA. ✉e-mail: ys776@cornell.edu

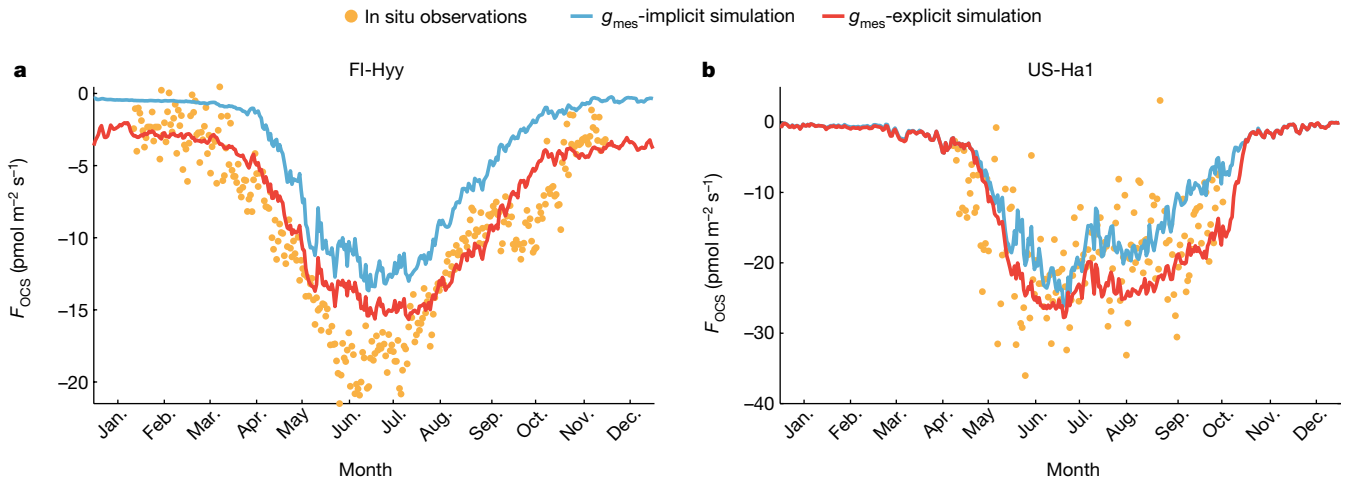

Fig. 1 | Comparison of simulated terrestrial ecosystem OCS fluxes with site observations. a,**b**, Comparison of seasonal cycles of terrestrial ecosystem OCS fluxes (F_{OCS}) simulated by implicit and explicit representations of mesophyll conductance (g_{mes}^{OCS}) with in situ ecosystem-scale measurements at FI-Hyy (**a**) and US-Ha1 (**b**). Negative F_{OCS} denotes net OCS uptake by the ecosystem.

An explicit implementation of g_{mes} is therefore essential to mechanistically resolve the internal drawdown of CO_2 and OCS along the mesophyll diffusion pathway. Although ad hoc compensating strategies using parameter tuning were used (or g_{mes}-implicit) and have seemed reasonable for estimating the 'mean' for contemporary periods over limited spatial areas, such strategies may fall short in characterizing seasonal, interannual or long-term trends and spatial variability[24]. The impact of g_{mes} on the temporal and spatial dynamics of plant OCS uptakes and on OCS-inferred GPP estimates remains unclear.

In this study, we quantify global plant OCS uptake and GPP and map their spatiotemporal dynamics using a bottom-up, process-based approach. We incorporate mechanistic models of g_{mes} (ref. 24) and OCS diffusion[16] into National Center for Atmospheric Research Community Land Model version 5 (CLM5; Methods). We verify estimates of both OCS uptake and GPP against independent measurements and inferences from the field to the global scale. A key advantage of our approach is to resolve the spatiotemporal patterns of GPP, with new insights beyond a single global constraint offered by ^{18}O (ref. 7) or soil respiration[8].

Impact of g_{mes} on OCS flux

Compared with the g_{mes}-implicit treatment, an explicit mechanistic representation of g_{mes} improves agreement in ecosystem OCS fluxes (F_{OCS}; negative for net uptake) with in situ measurements at both Hyytiälä Forest, Finland (FI-Hyy) and Harvard Forest, USA (US-Ha1), the only two sites for which multi-year, continuous ecosystem OCS flux measurements are available (Methods, Fig. 1 and Supplementary Fig. 1). In particular, the g_{mes}-explicit simulation better captures not only the peak-season magnitude but also the seasonal dynamics of F_{OCS}. For example, at FI-Hyy, in situ F_{OCS} reveals that OCS uptake may start as early as the end of January (for example, in 2017; Supplementary Fig. 1). This early start is unlikely to be a consequence of soil OCS uptake because the soil temperature was too low to stimulate soil uptake (Supplementary Fig. 2). The g_{mes}-explicit simulation more realistically captures this early start of active F_{OCS} uptake. Moreover, in the spring and autumn at both FI-Hyy and US-Ha1, the g_{mes}-explicit simulated F_{OCS} agrees well with measurements; by contrast, the g_{mes}-implicit simulation underestimates F_{OCS} in both spring and autumn at both sites.

The improved model–observation consistencies in F_{OCS} result from an explicit consideration of g_{mes}^{OCS}. This is confirmed by examining the internal conductance of OCS from the leaf substomatal cavity to the OCS consumption site (g_i^{OCS}) and the overall conductance of OCS from ambient air to the OCS consumption site (g_t^{OCS}; Methods). The g_{mes}-implicit strategy bundles g_{mes}^{OCS} and g_{CA}^{OCS} to form an apparent internal OCS conductance (g_i^{OCS}) and ties it empirically to the maximum carboxylation rate (V_{cmax}) through a fixed scaling factor α (Methods)[16]. However, the actual relationship between g_i^{OCS} and V_{cmax} may vary with environmental conditions and phenological stages[25] beyond what the limited existing observations of gas exchange can constrain[16]. Taking the two sites as an example, the V_{cmax}-scaled g_i^{OCS} and the resulting g_t^{OCS} tend to be smaller than those calculated from g_{mes}^{OCS} and g_{CA}^{OCS} explicitly considered throughout the year, especially in the dormant and shoulder seasons (Supplementary Fig. 3). By contrast, the g_{mes}-explicit g_t^{OCS} more closely matches in situ measurements (Supplementary Fig. 3). These results indicate that parameter adjustment cannot compensate for a lack of mechanistic representation of g_{mes}^{OCS} (Supplementary Fig. 4). Although the peak F_{OCS} can be matched by tuning the scaling factor α (ref. 25), such tuning cannot reproduce the seasonal variations of F_{OCS} (Supplementary Fig. 1), particularly in the shoulder and dormant seasons because V_{cmax} decreases faster than g_i^{OCS} does (Supplementary Fig. 4). A similar phenomenon occurs at night when carboxylation pauses while leaf stomata remain partially open, allowing sizeable plant OCS uptake that amounts to 20–30% of the total daily uptake[26–28]. Such night-time plant OCS uptake cannot be captured by the g_{mes}-implicit strategy, but can be reproduced by the g_{mes}-explicit simulation (Supplementary Fig. 5). Note that both g_{mes}-implicit and g_{mes}-explicit simulations assume that OCS is predominantly consumed by CA within leaf chloroplasts[29].

Globally, g_{mes}-implicit and g_{mes}-explicit simulations of F_{OCS} show remarkable differences in time and space (Fig. 2 and Supplementary Fig. 6). Implicit g_{mes} modelling leads to a weaker F_{OCS} for almost all plant functional types (PFTs; Fig. 2) but C_3 arctic grass. From 2000 to 2010, the g_{mes}-implicit simulation yields a global average OCS sink of 752 GgS yr^{-1}, consistent with the SiB4 estimate of 753 GgS yr^{-1} (ref. 25). The g_{mes}-explicit simulation yields a global F_{OCS} of 967 GgS yr^{-1}, which is still within the range of 368–1,279 GgS yr^{-1} (with a mean of 917 GgS yr^{-1}) reported previously (Supplementary Fig. 6). Differences between the g_{mes}-explicit and g_{mes}-implicit simulations (ΔF_{OCS}), generally around 30–50%, persist throughout the year for temperate and tropical regions but exhibit the largest seasonal variation in boreal forests of the Northern Hemisphere. The distinct seasonal variation of ΔF_{OCS} in boreal forests indicates a longer active OCS uptake period by g_{mes}-explicit than g_{mes}-implicit simulations, consistent with in situ measurements at FI-Hyy (Fig. 1 and Supplementary Fig. 1). The most pronounced g_{mes} impact on F_{OCS} is concentrated in Northern Hemisphere boreal forests

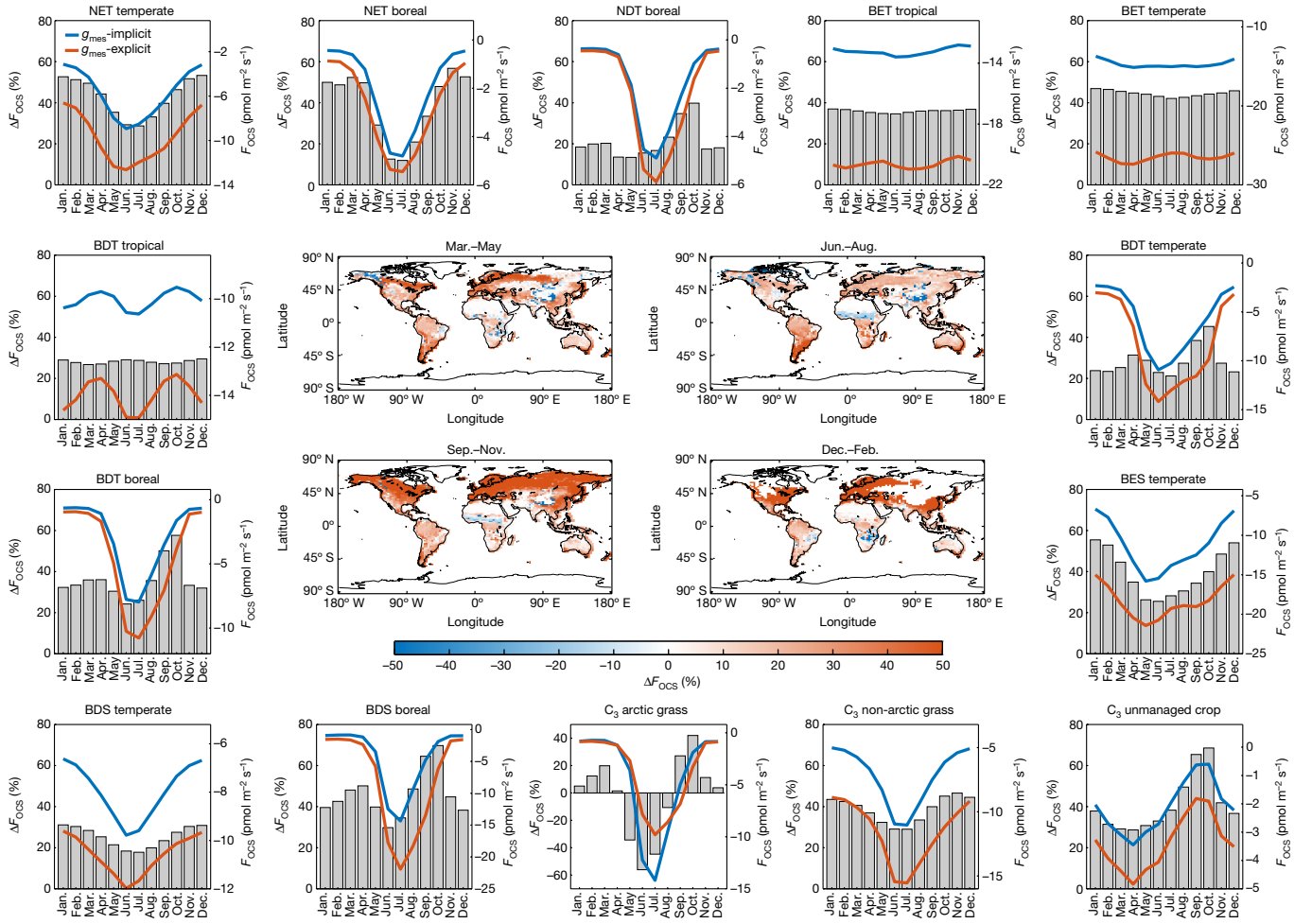

Fig. 2 | Comparison of F_{OCS} (2000–2010 average) between g_{mes}-implicit and g_{mes}-explicit simulations across PFTs. Curves show monthly mean F_{OCS} (the right ordinate), and bars denote relative difference in percentage (ΔF_{OCS}, g_{mes}-explicit minus g_{mes}-implicit, normalized by g_{mes}-explicit F_{OCS}; the left ordinate). Maps show the seasonal ΔF_{OCS} across the globe. A positive ΔF_{OCS} indicates larger ecosystem OCS uptake (or sink) in g_{mes}-explicit simulations. BDS, broadleaf deciduous shrub; BDT, broadleaf deciduous tree; BES, broadleaf evergreen shrub; BET, broadleaf evergreen tree; NDT, needleleaf deciduous tree; NET, needleleaf evergreen tree. Global PFT distribution is shown in Supplementary Fig. 16.

because of their stronger mesophyll diffusion limitation (that is, smaller g_{mes}) than other PFTs[24] (Supplementary Fig. 7). For these PFTs, g_{mes} acts as a strong barrier to both OCS and CO_2 diffusion, decreasing F_{OCS} by 10% to 50% (Supplementary Fig. 8) and potentially reducing photosynthesis by 25% to 75% according to leaf-level studies[30]. Although the arctic C_3 grass is the only PFT to show weaker F_{OCS} in the g_{mes}-explicit simulation, this pattern cannot yet be validated owing to scarce measurements from this PFT[31]. Future studies, such as measurements and modelling of g_{mes} dependence on leaf traits, temperature and other environmental conditions, are required to understand the impact of g_{mes} on F_{OCS} for this PFT.

Our results highlight the importance of mesophyll control, which is of a similar magnitude to stomatal control, but has not received due attention in TBM representation[24]. The global g_{mes} model used here formulates g_{mes} as a function of leaf dry mass per unit area (M_a), and considers its vertical variation within canopy depth (driven by light gradient) as well as its response to leaf temperature and water stress. This formulation characterizes the first-order impacts of leaf structure and environmental variations on g_{mes} and demonstrates reasonable performance in estimating contemporary GPP and OCS fluxes across spatial scales. However, future research to improve the g_{mes} model formulation is still needed, especially with regard to the varying relationship between g_{mes} and M_a across different PFTs[32], temperature response functions of g_{mes}[33], complex responses of g_{mes} to soil water stress[34], and acclimation to future environmental changes[35]. These complexities, although challenging to parameterize owing to limited measurements, are critical to understanding and predicting the g_{mes} impact on global carbon and water fluxes under future changing climate scenarios[20] (see discussion in Supplementary Text 1).

GPP inferred from OCS fluxes

Furthermore, we used leaf relative uptake (LRU; the concentration-normalized ratio of OCS and CO_2 uptake)[14,36] to translate plant OCS uptake into GPP. LRU varies with environmental conditions, particularly light intensities, among other factors (for example, water vapour pressure deficit (VPD))[26,37]. The authors of ref. 38 developed a parsimonious empirical equation between LRU and photosynthetically active radiation (PAR) based on hourly in situ measurements at FI-Hyy. This unique leaf-scale dataset paired LRU and PAR along a full range of PAR continuum. Its joint use with concurrent canopy-level OCS flux measurements facilitated scaling from leaf to canopy scales. We applied the LRU–PAR equation developed from this dataset (equation (25) and Supplementary Fig. 9) to translate the simulated plant OCS fluxes (g_{mes}-explicit) into GPP, denoted as $GPP_{OCS\_LRU\_PAR}$ (Methods).

We found that $GPP_{OCS\_LRU\_PAR}$ mirrors the in situ GPP partitioned from net ecosystem exchange of CO_2 (NEE) at both diurnal (Fig. 3) and seasonal (Supplementary Fig. 10) scales. Compared to GPP

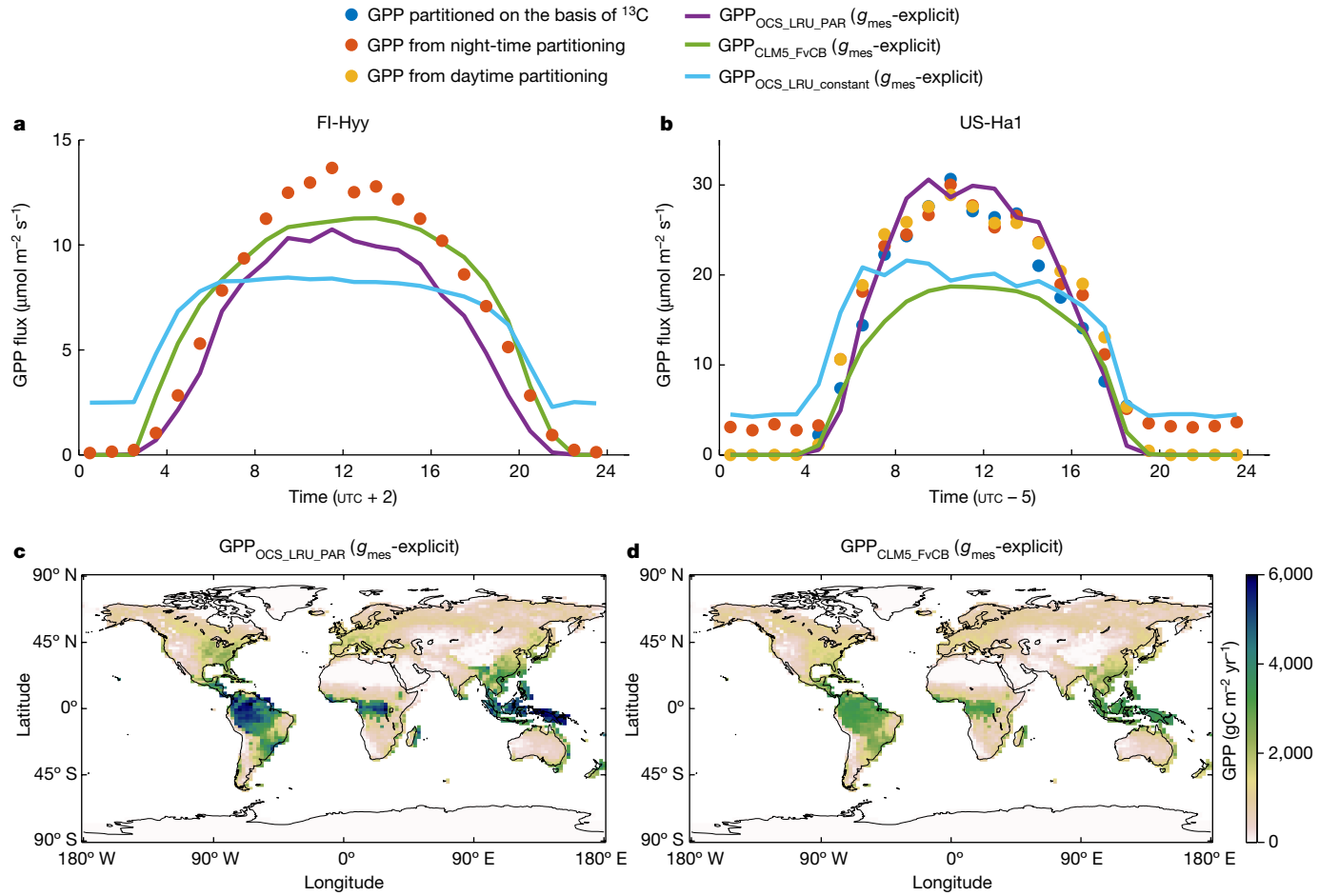

Fig. 3 | Comparison of GPP inferred from CLM5 OCS simulation with GPP simulated by CLM5 implemented with the default FvCB model. a,**b**, Diurnal patterns of CLM5 OCS-inferred GPP ($GPP_{OCS\_LRU\_PAR}$ and $GPP_{OCS\_LRU\_constant}$, both are g_{mes}-explicit) and the CLM5 GPP simulations with the default FvCB (GPP_{CLM5_FvCB}, g_{mes}-explicit) in comparison to GPP partitioned from in situ NEE (detailed partitioning methods described in Supplementary Table 3) at FI-Hyy (**a**) and US-Ha1 (**b**). Owing to data availability, the mean diurnal cycle from June to mid-July 2017 is shown for FI-Hyy, and that from June to August during 2012 and 2013 is shown for US-Ha1. **c**,**d**, Global annual mean GPP (in 2010) inferred from CLM5 OCS simulations (**c**) and simulated by CLM5 with default FvCB (**d**), respectively.

inferred from plant OCS uptake with a commonly used constant LRU value (1.61 for C_3 (ref. 39); $GPP_{OCS\_LRU\_constant}$, g_{mes}-explicit), GPP derived from PAR-dependent LRU ($GPP_{OCS\_LRU\_PAR}$) is higher during daytime and the growing season, but zero at night-time and lower during the non-growing season as expected. $GPP_{OCS\_LRU\_PAR}$ tracks the diurnal and seasonal dynamics of in situ GPP more closely than $GPP_{OCS\_LRU\_constant}$. In addition, $GPP_{OCS\_LRU\_PAR}$ outperforms GPP simulated by the default Farquhar, von Caemmerer and Berry (FvCB) model implemented in CLM5 (GPP_{CLM5_FvCB}). For example, GPP_{CLM5_FvCB} fails to capture the diurnal shape of GPP at FI-Hyy and US-Ha1 (for example, the hysteresis in the afternoon; Fig. 3), and markedly underestimates daytime and growing-season GPP at US-Ha1 (Fig. 3b and Supplementary Fig. 10c).

At the global scale, applying the parsimonious LRU–PAR equation (Methods) leads to an annual GPP estimate of 157 (± 8.5) PgC yr^{-1} ($GPP_{OCS\_LRU\_PAR}$, g_{mes}-explicit, the 2000–2010 average; Fig. 4a and Supplementary Fig. 11). Implicit treatment of g_{mes} only slightly changes the global annual mean GPP to 152 PgC yr^{-1} (Supplementary Table 1), implying that compensatory parameter adjustment might match the present-day global annual GPP magnitude but can distort the simulated seasonal and spatial dynamics of OCS fluxes and thus GPP (Fig. 2). However, a constant LRU value (a simplified strategy adopted in the literature[10,14]) strongly affects the global GPP estimates (Fig. 4a, Supplementary Table 1 and detailed discussion in Supplementary Text 2).

The global annual mean GPP inferred from the ^{18}O signature of atmospheric CO_2 was 150–175 PgC yr^{-1} (ref. 7) and that inferred from soil respiration was 149^{+29}_{-23} PgC yr^{-1} (ref. 8). Our estimate of 157 (±8.5) PgC yr^{-1}, inferred from plant OCS uptake, falls within these independent constraints but with a considerably narrower uncertainty range. However, all of these estimates are much higher than those derived from satellite optical remote sensing (for example, estimates from upscaling globally distributed flux tower measurements using machine learning[5,40] or light use efficiency models[13,41]; Fig. 4a and Supplementary Fig. 11). Recently, higher GPP estimates (120–140 PgC yr^{-1}) were obtained from satellite solar-induced fluorescence (SIF) remote sensing with the assumption of a linear SIF–GPP scaling[42], and process-based models driven by satellite optical data (for example, leaf area index, fraction of PAR and vegetation indices)[43,44]; these estimates are still lower than our OCS-inferred GPP estimates. The generally lower existing estimates probably result from their shared biases or uncertainties such as the spatial representativeness of flux towers, NEE partitioning approaches and uncertainties in satellite remote sensing products, among others (detailed discussion in Supplementary Text 3). The global annual mean GPP directly simulated by CLM5 with the default FvCB photosynthesis module (GPP_{CLM5_FvCB}) is 126 PgC yr^{-1}, similar to estimates by existing satellite optical data-driven products. This low estimate probably results from parameter tuning to reproduce the widely cited bottom-up GPP estimates (for example, around 120 PgC yr^{-1})[4,5]. Our stronger

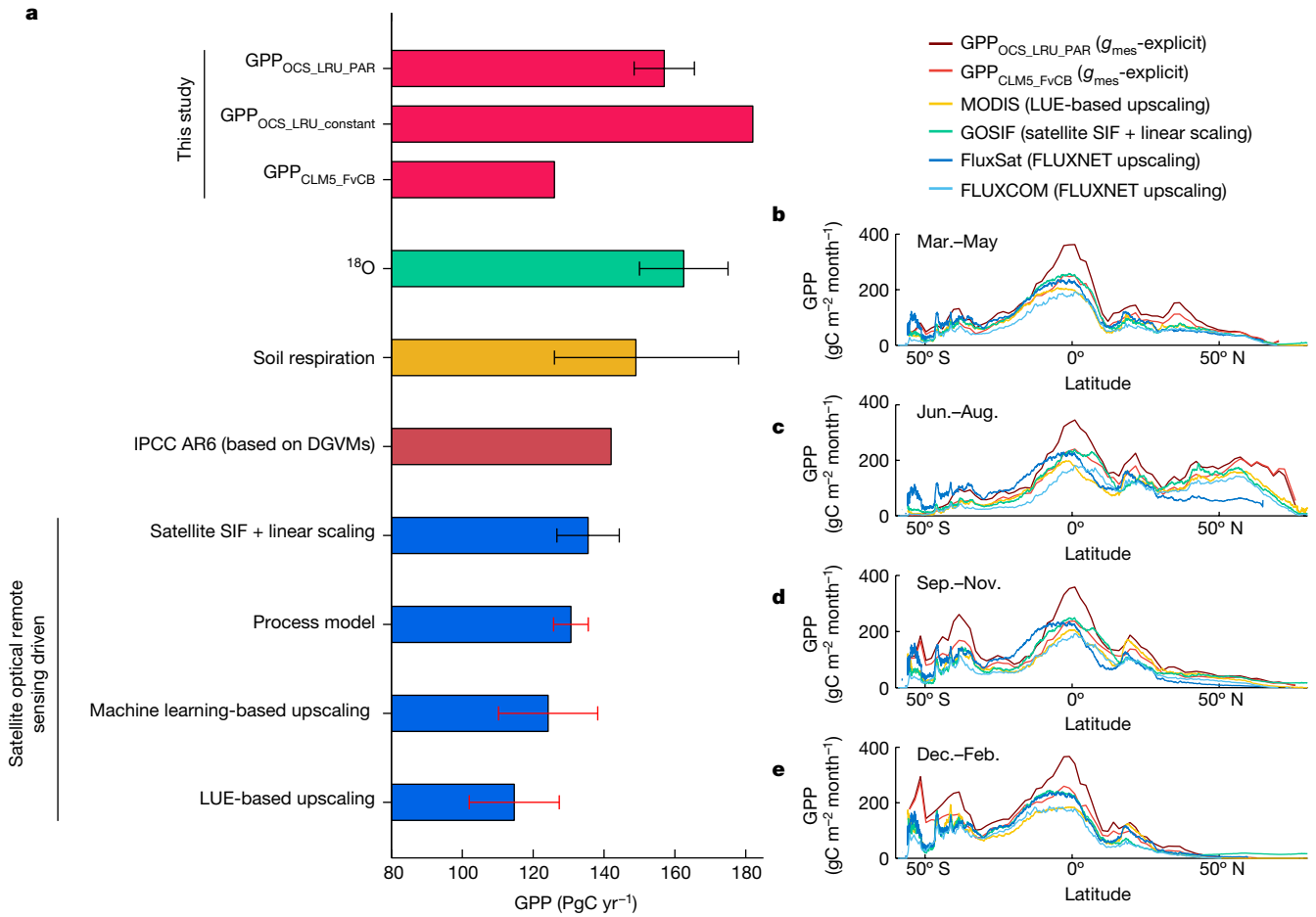

Fig. 4 | Intercomparison of GPP estimates from existing approaches. a, The global annual mean GPP estimates synthesized from literature[8]. A full list of individual studies under each category is available in Supplementary Fig. 11 (with references). The colours of the bars differentiate the broad categories of approaches. GPP estimates from this study are all based on g_{mes}-explicit simulations. GPP estimates inferred from ^{18}O, soil respiration and satellite SIF with linear scaling come from single references; thus, the error bars (in black) denote their uncertainty ranges provided by each reference. GPP estimates from upscaling based on machine learning or light use efficiency (LUE) and those from process based models are synthesized from multiple references and the error bars (in red) denote the standard deviation across different studies falling into the same category of approaches. IPCC AR6, Intergovernmental Panel on Climate Change Sixth Assessment Report; DGVMs, dynamic global vegetation models. **b**–**e**, Zonal variations of GPP from this study and a subset of widely used satellite optical remote sensing-driven products from **a**.

OCS-inferred GPP estimate is not due to the lack of exceptional El Niño/Southern Oscillation events in the period from 2000 to 2010, as demonstrated by our sensitivity simulation (Supplementary Text 4 and Supplementary Fig. 12).

Revisiting the spatial GPP patterns

Plant OCS uptake can offer new insights into the spatial and temporal variations of GPP, which previous global constraints such as ^{18}O (ref. 7) and soil respiration[8] were unable to resolve. Our OCS-based approach not only informs global GPP but also pinpoints where and when GPP is probably misrepresented in existing remote sensing-based products. To discern the spatiotemporal disparities of GPP from different approaches, we selected four widely used satellite optical remote sensing-driven GPP products (that is, MODIS[45], GOSIF[46], FluxSat[41] and FLUXCOM[5] GPP) and compared them with our OCS-inferred GPP; Fig. 4b–e and Supplementary Fig. 13). The largest discrepancies occur in the pan-tropical rainforests. This finding is consistent with a recent study[11] that estimated GPP from comprehensive plot-scale measurements and detailed carbon budget quantification[47]. The aforementioned study reported that the mature intact rainforests in the tropical Amazon have substantially stronger GPP than what the existing satellite optical remote sensing-driven products indicated. The poor performance of these satellite GPP products in the tropics is probably due to the impacts of frequent clouds and scarcity of flux tower observations that are needed for upscaling in this most productive region of the Earth[6].

To evaluate the robustness of the OCS-inferred GPP estimates in the pan-tropics, we compared GPP$_{OCS_LRU_PAR}$ against in situ data at four tropical flux tower sites located in the central and eastern Amazon[48] (Supplementary Table 2). We found a close agreement in both dry and wet seasons at the four sites, particularly at the K67 and CAX towers (Supplementary Fig. 14 and Supplementary Table 2). Additionally, GPP$_{OCS_LRU_PAR}$ outperforms GPP$_{CLM5_FvCB}$ (both g_{mes}-implicit and g_{mes}-explicit), which substantially underestimates GPP at all four sites in both dry and wet seasons (Supplementary Fig. 14). Furthermore, GPP$_{OCS_LRU_PAR}$ reveals substantially higher productivity in the western than central Amazon, as expected from the tropical forest aridity gradient there[11]. Such a contrast is consistent with OCO-2 SIF observations[49] and inference from plot-scale measurements[11] but not captured by GPP$_{CLM5_FvCB}$ (Fig. 3c,d) or other GPP data products (Supplementary Fig. 13). These emergent patterns have important implications on the carbon sink capacity of tropical rainforests and their resilience to stress under climate change, and thus should be thoroughly evaluated in the future with independent

ecosystem-scale measurements of OCS and GPP fluxes. Our findings suggest that in situ measurements of ecosystem-scale OCS uptake with concurrent CO_2 fluxes are critically needed across the pan-tropics to understand their dynamical relationships, which ultimately will help verify the regional-scale GPP magnitude and spatiotemporal variations reported here.

Furthermore, current satellite-driven products also underestimate GPP in Northern Hemisphere mid-to-high latitudes, particularly during the growing season (Fig. 4c). This pattern is consistent with previous findings[50] that utilized atmospheric OCS concentrations from ground measurements and aircraft campaigns to reveal a stronger GPP than existing TBMs in Northern Hemisphere high latitudes.

Impact of LRU on OCS-inferred GPP

LRU, a key parameter for OCS-based GPP inference, varies with VPD[26,38] and with PFTs[17,39]; yet this variability cannot be fully constrained owing to limited observations. Nevertheless, our simulations and uncertainty quantification indicate that the empirical LRU–PAR equation is broadly applicable across species. For example, GPP estimates based on the LRU–PAR relationship derived at FI-Hyy track the GPP diurnal and seasonal cycles at US-Ha1 reasonably well (Fig. 3b and Supplementary Fig. 10c,d). Even in the tropical Amazon with markedly different environments, this parsimonious equation still leads to a GPP magnitude and dry–wet contrast consistent with in situ measurements (Supplementary Fig. 14). At the global scale, we used a Monte Carlo approach to quantifying the potential uncertainty from cross-PFT variability in LRU and in the LRU dependency on PAR. We synthesized field and laboratory measurements[38,39] as a guidance to generate an ensemble of PFT-specific LRU–PAR relationships that mimic a diverse combination of PFT-dependent LRU–PAR relationships (details in Methods and Supplementary Text 5). The ensemble encompasses a wide range of LRU under ambient light conditions (Supplementary Fig. 15), but still yields a highly constrained uncertainty range of global GPP (that is, ±8.5 PgC yr^{-1}; Fig. 4). This indicates that the sensitivity of the global annual GPP estimates to the cross-PFT variability in LRU and the LRU–PAR relationship is scale-dependent. At local scales, this sensitivity can be substantial, as documented by chamber and/or canopy-level measurements[38,51], but at the global scale, such sensitivity greatly diminishes. The dearth of field observations under varying light intensities and other environmental gradients across diverse biomes or species prevents a PFT-specific LRU formulation that varies not only with PAR but also with other environmental conditions (for example, VPD[26]). Field measurements across a diverse range of biomes and environments are urgently needed to characterize PFT- and species-specific LRU dependency on environmental conditions and plant traits.

Conclusions

Taking advantage of the close coupling between OCS and CO_2 diffusion processes, we investigated the impact of mesophyll diffusion on the dynamics of plant OCS uptake, and inferred the global GPP and its spatiotemporal patterns. Our bottom-up estimates of plant OCS fluxes provide robust priors for quantifying the global OCS budget and for ascertaining the sources and sinks of OCS on Earth with inversion approaches[10,50]. Harnessing the mechanistic constraint from plant OCS uptake on photosynthesis, our study provides a well-constrained contemporary GPP estimate. This new estimate is consistent with independent inferences from ^{18}O and soil respiration but with a much-improved confidence level and fully resolved spatial and temporal dynamics. Our advances mark a key step towards constraining GPP dynamics. As GPP is a primary determinant of terrestrial carbon sinks and shapes climate trajectories, our findings lay a solid physiological foundation on which the understanding and prediction of carbon–climate feedbacks can be advanced.

Online content

Any methods, additional references, Nature Portfolio reporting summaries, source data, extended data, supplementary information, acknowledgements, peer review information; details of author contributions and competing interests; and statements of data and code availability are available at https://doi.org/10.1038/s41586-024-08050-3.

1. Anav, A. et al. Spatiotemporal patterns of terrestrial gross primary production: a review. *Rev. Geophys.* **53**, 785–818 (2015).
2. Trabalka, J. R. *Atmospheric Carbon Dioxide and the Global Carbon Cycle* (US Department of Energy, 1986).
3. Bolin, B. & Fung, I. *The Carbon Cycle Revisited* Vol. 3 (University Corp. for Atmospheric Research, 1992).
4. Beer, C. et al. Terrestrial gross carbon dioxide uptake: global distribution and covariation with climate. *Science* **329**, 834–838 (2010).
5. Jung, M. et al. Scaling carbon fluxes from eddy covariance sites to globe: synthesis and evaluation of the FLUXCOM approach. *Biogeosciences* **17**, 1343–1365 (2020).
6. Ryu, Y., Berry, J. A. & Baldocchi, D. D. What is global photosynthesis? History, uncertainties and opportunities. *Remote Sens. Environ.* **223**, 95–114 (2019).
7. Welp, L. R. et al. Interannual variability in the oxygen isotopes of atmospheric CO_2 driven by El Niño. *Nature* **477**, 579–582 (2011).
8. Jian, J. et al. Historically inconsistent productivity and respiration fluxes in the global terrestrial carbon cycle. *Nat. Commun.* **13**, 1733 (2022).
9. Friedlingstein, P. et al. Climate–carbon cycle feedback analysis: results from the C4MIP model intercomparison. *J. Clim.* **19**, 3337–3353 (2006).
10. Campbell, J. E. et al. Large historical growth in global terrestrial gross primary production. *Nature* **544**, 84–87 (2017).
11. Zhang-Zheng, H. et al. Contrasting carbon cycle along tropical forest aridity gradients in West Africa and Amazonia. *Nat. Commun.* **15**, 3158 (2024).
12. Canadell, J. G. et al. In *Climate Change 2021: The Physical Science Basis* (ed. Brovkin, V.) Ch. 5 (Cambridge Univ. Press, 2021).
13. Chen, M. et al. Regional contribution to variability and trends of global gross primary productivity. *Environ. Res. Lett.* **12**, 105005 (2017).
14. Hilton, T. W. et al. Peak growing season gross uptake of carbon in North America is largest in the Midwest USA. *Nat. Clim. Change* **7**, 450–454 (2017).
15. Friedlingstein, P. et al. Global carbon budget 2023. *Earth Syst. Sci. Data* **15**, 5301–5369 (2023).
16. Berry, J. et al. A coupled model of the global cycles of carbonyl sulfide and CO_2: a possible new window on the carbon cycle. *J. Geophys. Res. Biogeosci.* **118**, 842–852 (2013).
17. Whelan, M. E. et al. Reviews and syntheses: carbonyl sulfide as a multi-scale tracer for carbon and water cycles. *Biogeosciences* **15**, 3625–3657 (2018).
18. Wehr, R. et al. Dynamics of canopy stomatal conductance, transpiration, and evaporation in a temperate deciduous forest, validated by carbonyl sulfide uptake. *Biogeosciences* **14**, 389–401 (2017).
19. Medlyn, B. E. et al. Reconciling the optimal and empirical approaches to modelling stomatal conductance. *Glob. Chang. Biol.* **17**, 2134–2144 (2011).
20. Knauer, J. et al. Mesophyll conductance in land surface models: effects on photosynthesis and transpiration. *Plant J.* **101**, 858–873 (2020).
21. Sun, Y. et al. Asymmetrical effects of mesophyll conductance on fundamental photosynthetic parameters and their relationships estimated from leaf gas exchange measurements. *Plant Cell Environ.* **37**, 978–994 (2014).
22. Jähne, B., Heinz, G. & Dietrich, W. Measurement of the diffusion coefficients of sparingly soluble gases in water. *J. Geophys. Res.* **92**, 10767–10776 (1987).
23. Ulshöfer, V. S., Flock, O. R., Uher, G. & Andreae, M. O. Photochemical production and air-sea exchange of carbonyl sulfide in the eastern Mediterranean Sea. *Mar. Chem.* **53**, 25–39 (1996).
24. Sun, Y. et al. Impact of mesophyll diffusion on estimated global land CO2 fertilization. *Proc. Natl Acad. Sci. USA* **111**, 15774–15779 (2014).
25. Kooijmans, L. M. J. et al. Evaluation of carbonyl sulfide biosphere exchange in the Simple Biosphere Model (SiB4). *Biogeosciences* **18**, 6547–6565 (2021).
26. Sun, W., Maseyk, K., Lett, C. & Seibt, U. Stomatal control of leaf fluxes of carbonyl sulfide and CO_2 in a Typha freshwater marsh. *Biogeosciences* **15**, 3277–3291 (2018).
27. Maseyk, K. et al. Sources and sinks of carbonyl sulfide in an agricultural field in the Southern Great Plains. *Proc. Natl Acad. Sci. USA* **111**, 9064–9069 (2014).
28. Kooijmans, L. M. J. et al. Canopy uptake dominates nighttime carbonyl sulfide fluxes in a boreal forest. *Atmos. Chem. Phys.* **17**, 11453–11465 (2017).
29. Stimler, K., Berry, J. A., Montzka, S. A. & Yakir, D. Association between carbonyl sulfide uptake and 18D during gas exchange in C3 and C4 leaves. *Plant Physiol.* **157**, 509–517 (2011).
30. Terashima, I., Hanba, Y. T., Tazoe, Y., Vyas, P. & Yano, S. Irradiance and phenotype: comparative eco-development of sun and shade leaves in relation to photosynthetic CO_2 diffusion. *J. Exp. Bot.* **57**, 343–354 (2006).
31. Niinemets, U., Díaz-Espejo, A., Flexas, J., Galmés, J. & Warren, C. R. Role of mesophyll diffusion conductance in constraining potential photosynthetic productivity in the field. *J. Exp. Bot.* **60**, 2249–2270 (2009).
32. Niinemets, U., Wright, I. J. & Evans, J. R. Leaf mesophyll diffusion conductance in 35 Australian sclerophylls covering a broad range of foliage structural and physiological variation. *J. Exp. Bot.* **60**, 2433–2449 (2009).
33. Bernacchi, C. J., Portis, A. R., Nakano, H., von Caemmerer, S. & Long, S. P. Temperature response of mesophyll conductance. Implications for the determination of Rubisco enzyme kinetics and for limitations to photosynthesis in vivo. *Plant Physiol.* **130**, 1992–1998 (2002).

34. Cano, F. J., López, R. & Warren, C. R. Implications of the mesophyll conductance to CO_2 for photosynthesis and water-use efficiency during long-term water stress and recovery in two contrasting Eucalyptus species. *Plant Cell Environ.* **37**, 2470–2490 (2014).
35. Dillaway, D. N. & Kruger, E. L. Thermal acclimation of photosynthesis: a comparison of boreal and temperate tree species along a latitudinal transect. *Plant Cell Environ.* **33**, 888–899 (2010).
36. Campbell, J. E. et al. Photosynthetic control of atmospheric carbonyl sulfide during the growing season. *Science* **322**, 1085–1088 (2008).
37. Stimler, K., Montzka, S. A., Berry, J. A., Rudich, Y. & Yakir, D. Relationships between carbonyl sulfide (COS) and CO_2 during leaf gas exchange. *New Phytol.* **186**, 869–878 (2010).
38. Kooijmans, L. M. J. et al. Influences of light and humidity on carbonyl sulfide-based estimates of photosynthesis. *Proc. Natl Acad. Sci. USA* **116**, 2470–2475 (2019).
39. Stimler, K., Berry, J. A. & Yakir, D. Effects of carbonyl sulfide and carbonic anhydrase on stomatal conductance. *Plant Physiol.* **158**, 524–530 (2012).
40. Jung, M. et al. Global patterns of land-atmosphere fluxes of carbon dioxide, latent heat, and sensible heat derived from eddy covariance, satellite, and meteorological observations. *J. Geophys. Res.* **116**, G00J07 (2011).
41. Joiner, J. et al. Estimation of terrestrial global gross primary production (GPP) with satellite data-driven models and eddy covariance flux data. *Remote Sens.* **10**, 1346 (2018).
42. Li, X. & Xiao, J. Mapping photosynthesis solely from solar-induced chlorophyll fluorescence: a global, fine-resolution dataset of gross primary production derived from OCO-2. *Remote Sens.* **11**, 2563 (2019).
43. Chen, J. M. et al. Effects of foliage clumping on the estimation of global terrestrial gross primary productivity. *Glob. Biogeochem. Cycles* **26**, GB1019 (2012).
44. Jiang, C. & Ryu, Y. Multi-scale evaluation of global gross primary productivity and evapotranspiration products derived from Breathing Earth System Simulator (BESS). *Remote Sens. Environ.* **186**, 528–547 (2016).
45. Running, S. W. et al. A continuous satellite-derived measure of global terrestrial primary production. *Bioscience* **54**, 547–560 (2004).
46. Li, X. & Xiao, J. A global, 0.05-degree product of solar-induced chlorophyll fluorescence derived from OCO-2, MODIS, and reanalysis data. *Remote Sens.* **11**, 517 (2019).
47. Malhi, Y. et al. The Global Ecosystems Monitoring network: monitoring ecosystem productivity and carbon cycling across the tropics. *Biol. Conserv.* **253**, 108889 (2021).
48. Restrepo-Coupe, N. et al. Do dynamic global vegetation models capture the seasonality of carbon fluxes in the Amazon basin? A data-model intercomparison. *Glob. Change Biol.* **23**, 191–208 (2017).
49. Worden, J. et al. Satellite observations of the tropical terrestrial carbon balance and interactions with the water cycle during the 21st century. *Rev. Geophys.* **59**, e2020RG000711 (2021).
50. Kuai, L. et al. Quantifying northern high latitude gross primary productivity (GPP) using carbonyl sulfide (OCS). *Glob. Biogeochem. Cycles* **36**, e2021GB007216 (2022).
51. Commane, R. et al. Seasonal fluxes of carbonyl sulfide in a midlatitude forest. *Proc. Natl Acad. Sci. USA* **112**, 14162–14167 (2015).

Methods

Model parameterization of ecosystem OCS fluxes

Ecosystem OCS uptake. Terrestrial ecosystem OCS uptake (termed F_{OCS}) is modelled as:

$$F_{OCS} = g_a^{OCS}(OCS_a - OCS_m) \quad (1)$$

in which g_a^{OCS} is the aerodynamic conductance for OCS and is assumed to be equal to that for water; OCS_a is the OCS concentration in the canopy air space, updated at each model time step; OCS_m is the OCS concentration at a reference level. We used the global gridded monthly estimations of OCS concentration from ref. 52.

OCS_a in equation (1) was updated at each time step on the basis of simulated plant and soil fluxes as follows:

$$OCS_a = \left(OCS_{a\_prev} + dt/OCS_{cap} \times \left(OCS_m \times g_a^{OCS} - F_{ocs\_soil} - F_{ocs\_veg}\right)\right) \Big/ \left(1 + dt \times g_a^{OCS}/OCS_{cap}\right) \quad (2)$$

in which OCS_{a_prev} refers to OCS_a in the previous time step (the OCS concentration at the starting time step was set as 450 parts per trillion); dt is the CLM5 model time step; OCS_{cap} is the air capacity for the OCS exchange (with the unit of moles of air per square metre), calculated on the basis of OCS canopy air depth, which was assumed to be a constant (that is, 10 m); F_{ocs_soil} and F_{ocs_veg} are the OCS plant and soil fluxes whose calculation is described below.

OCS plant uptake. Plant uptake of OCS (termed as F_{ocs_veg}) is modelled as:

$$F_{ocs\_veg} = OCS_a \times g_t^{OCS}; g_t^{OCS} = \frac{1}{\frac{1}{g_b^{OCS}} + \frac{1}{g_s^{OCS}} + \frac{1}{g_{mes}^{OCS}} + \frac{1}{g_{CA}^{OCS}}} \quad (3)$$

in which OCS_a was updated for each model time step by equation (2), g_t^{OCS} is the OCS conductance from the leaf boundary layer to the CA reaction site (with the unit of moles per square metre per second), calculated on the basis of leaf boundary layer conductance (g_b^{OCS}), stomatal conductance (g_s^{OCS}) and mesophyll conductance (g_{mes}^{OCS}), as well as a reaction rate coefficient for OCS hydrolysis by CA (g_{CA}^{OCS}, also termed as biochemical conductance).

Although CA is ubiquitous in plants, we considered only the OCS consumption by chloroplast CA, as existing experimental evidence showed that chloroplast CA dominates the total OCS consumption[29]. Following existing parameterization of plant OCS uptake[16], we assumed that the pathway for OCS diffusion from ambient air to leaf chloroplast is similar to that of CO_2 as represented in current land surface models. Analogous to CO_2, the boundary layer and stomatal conductance of OCS can be scaled from those of water vapour (denoted as $g_s^{H_2O}$ and $g_b^{H_2O}$, respectively)[37] following:

$$g_b^{OCS} = \frac{g_b^{H_2O}}{1.56}, g_s^{OCS} = \frac{g_s^{H_2O}}{1.94} \quad (4)$$

The mesophyll conductance of OCS (g_{mes}^{OCS}) was assumed to be equal to that of CO_2 ($g_{mes}^{CO_2}$)[18], as a substantial part of mesophyll diffusion is in the aqueous phase, and the aqueous diffusivities of these two gases are similar[22,23]. However, unlike $g_s^{H_2O}$ and $g_b^{H_2O}$, $g_{mes}^{CO_2}$ was not represented in the standard version of CLM5. In this study, we implemented both implicit and explicit considerations of mesophyll diffusion to model the OCS plant uptake (see descriptions below).

CLM is a two-big-leaf model, which resolves canopy leaves into sunlit and shaded leaves. Therefore, g_t^{OCS} was calculated respectively for sunlit and shaded leaves and aggregated as follows:

$$g_t^{OCS} = g_{t\_sun}^{OCS} \times LAI_{sun} + g_{t\_sha}^{OCS} \times LAI_{sha} \quad (5)$$

in which $g_{t\_sun}^{OCS}$ and $g_{t\_sha}^{OCS}$ are the g_t^{OCS} for sunlit and shaded leaves, respectively, and LAI_{sun} and LAI_{sha} are the leaf area index for sunlit and shaded leaves, respectively.

OCS plant model with implicit mesophyll diffusion. Independent studies have shown that both the mesophyll conductance (g_{mes}^{OCS}) and CA activity (g_{CA}^{OCS}) tend to scale with the maximum carboxylation rate of Rubisco (V_{cmax})[53,54]. Therefore, an alternative approach was proposed to combine the two processes of g_{mes}^{OCS} and g_{CA}^{OCS} into a single apparent conductance g_i^{OCS} for the calculation of the overall conductance g_t^{OCS}:

$$g_t^{OCS} = \frac{1}{\frac{1}{g_b^{OCS}} + \frac{1}{g_s^{OCS}} + \frac{1}{g_i^{OCS}}} \quad (6)$$

In equation (6), g_i^{OCS} represents the internal conductance of OCS diffusion from the intercellular air space to CA reaction sites and is assumed to be proportional to V_{cmax} (ref. 16):

$$g_i^{OCS} = \alpha \times V_{cmax} \times f_w(\theta) \times \left(\frac{p}{p_0}\right) \times \left(\frac{T_{can}}{T_0}\right) \quad (7)$$

in which α is a scaling factor (1,400 for C_3 species and 8,862 for C_4 species[25]); $f_w(\theta)$ is the water stress function (ranging from 0 to 1) implemented in CLM5; p is the atmospheric pressure; p_0 is the reference surface pressure (1,000 hPa); T_{can} is the canopy temperature, which is prognostically calculated by CLM5; and T_0 is the reference temperature (273.15 K). The water stress function $f_w(\theta)$ is:

$$f_w(\theta) = \sum_i^n f_{root,i} \times w_i(\theta) \quad (8)$$

in which $f_{root,i}$ denotes the root fraction within soil layer i; and w_i refers to the plant wilting factor related to soil water content θ.

OCS plant model with explicit mesophyll diffusion. Although mesophyll diffusion was not represented in the standard version of CLM5, attempts have been made to represent the mesophyll conductance of CO_2 ($g_{mes}^{CO_2}$)[24] in some ways. Here we assumed $g_{mes}^{CO_2}$ to be equal to g_{mes}^{OCS} (ref. 18), and leveraged a process-based g_{mes} model[24] to explicitly calculate g_{mes}. g_{CA}^{OCS}, which depends on CA activity, is assumed to be constant (0.055 mol $m^{-2}s^{-1}$) following ref. 18:

$$g_{CA}^{OCS} = 0.055. \quad (9)$$

This value (0.055) was estimated from measurements made at US-Ha1, a temperate deciduous forest, but works well also at a boreal needleleaf forest site (FI-Hyy; Fig. 1). This cross-site applicability suggests that the simulated OCS fluxes may not be sensitive to the value of g_{CA}^{OCS}. We also evaluated the impact of the temperature dependence of g_{CA}^{OCS}, using equation (10), and found no notable effects on the simulated OCS fluxes (Supplementary Fig. 17).

$$g_{CA}^{OCS} = 0.8 \times 0.055 \times \exp\left(\frac{E_0}{R}\left(\frac{1}{T_{ref}} - \frac{1}{T_L}\right)\right) \quad (10)$$

in which E_0 is the activation energy (40 kJ mol^{-1}), R is the ideal gas constant (8.3145 J mol^{-1} K^{-1}), T_{ref} denotes the reference temperature (293 K), and T_L is leaf temperature, prognostically calculated by CLM5.

Process-based g_{mes} model. The authors of ref. 24 developed the first global process-based $g_{mes}^{CO_2}$ model for C_3 plants, which was successfully applied to CLM4.5. The model considered $g_{mes}^{CO_2}$ variations with leaf structures and environmental conditions (for example, temperature and water stress), following:

$$g_{\mathrm{mes}}^{\mathrm{CO_2}} = g_{\mathrm{max0}} \times f_{\mathrm{l}}(\mathrm{LAI}) \times f_{\mathrm{T}}(T_{\mathrm{L}}) \times f_{\mathrm{w}}(\theta) \quad (11)$$

in which g_{max0} is the maximum $g_{\mathrm{mes}}^{\mathrm{CO_2}}$ under non-stressed conditions (that is, the presence of ample soil water at 25 °C); $f_{\mathrm{l}}(\mathrm{LAI})$ refers to the vertical variation of $g_{\mathrm{mes}}^{\mathrm{CO_2}}$ as a function of LAI; $f_{\mathrm{T}}(T_{\mathrm{L}})$ represents the response function of g_{mes} to leaf temperature (T_{L}, calculated by CLM5); and $f_{\mathrm{w}}(\theta)$ is the water stress function given in equation (8). g_{max0} is given by

$$g_{\mathrm{max0}} = a \times M_{\mathrm{a0}}^{b} \quad (12)$$

in which M_{a0} represents the leaf dry mass per unit area (M_{a}; with the unit of grams per square metre) at the canopy top, which can be calculated as two times the inverse of the canopy-top specific leaf area $\mathrm{SLA_0}$ (a parameter in CLM5). In CLM5, M_{a} differs from $1/\mathrm{SLA_0}$ (with the unit of grams of carbon per square metre) by a factor of two, as the latter includes only carbon fraction; the carbon content is assumed to be 50% of leaf dry mass[24]. a and b are two constants ($a = 24.240338$, $b = -0.6509$)[24]. This gives $g_{\mathrm{mes}}^{\mathrm{CO_2}}$ the unit of moles per square metre per second per pascal, which can be converted to moles per square metre per second if multiplied by surface pressure.

As CLM5 divides the canopy leaves into sunlit and shaded fractions, the function f_{l} in equation (11) was also defined for sunlit ($f_{\mathrm{l\_sun}}$) and shaded ($f_{\mathrm{l\_sha}}$) fractions, respectively:

$$f_{\mathrm{l\_sun}}(\mathrm{LAI}) = \frac{k_{\mathrm{b}}}{k_{\mathrm{g}} + k_{\mathrm{b}}} \times \frac{1 - \exp[-(k_{\mathrm{g}} + k_{\mathrm{b}})\mathrm{LAI}]}{1 - \exp(-k_{\mathrm{b}} \times \mathrm{LAI})} \quad (13a)$$

$$f_{\mathrm{l\_sha}}(\mathrm{LAI}) = \frac{k_{\mathrm{b}}}{k_{\mathrm{g}}\left(k_{\mathrm{g}} + k_{\mathrm{b}}\right)} \frac{k_{\mathrm{b}} - \left(k_{\mathrm{g}} + k_{\mathrm{b}}\right)\exp\left(-k_{\mathrm{g}}\mathrm{LAI}\right) + k_{\mathrm{g}}\exp\left[-\left(k_{\mathrm{g}} + k_{\mathrm{b}}\right)\mathrm{LAI}\right]}{\exp(-k_{\mathrm{b}}\mathrm{LAI}) - 1 + k_{\mathrm{b}}\mathrm{LAI}} \quad (13b)$$

in which k_{b} is the direct beam extinction coefficient; k_{g} is a composite parameter with an empirical value of 0.08997.

The temperature response function $f_{\mathrm{T}}(T_{\mathrm{L}})$ in equation (11) is given by:

$$f_{\mathrm{T}}(T_{\mathrm{L}}) = \exp\left(\frac{c - \Delta H_{\mathrm{a}}/(R \times T_{\mathrm{L}})}{1 + \exp((\Delta S \times T_{\mathrm{L}} - \Delta H_{\mathrm{d}})/(R \times T_{\mathrm{L}}))}\right) \quad (14)$$

in which c is a scaling constant (20), ΔH_{a} is the activation energy (49.6×10^3 J mol^{-1}), R is the ideal gas constant, ΔS is an entropy term (1.4×10^3 J mol^{-1} K^{-1}), and ΔH_{d} is the deactivation energy (437.4×10^3 J mol^{-1}).

The authors of ref. 24 also applied the simulated $g_{\mathrm{mes}}^{\mathrm{CO_2}}$ to facilitate a more accurate photosynthetic estimation, as $\mathrm{CO_2}$ concentrations drop considerably along mesophyll diffusion pathways, expressed by equation (15):

$$C_{\mathrm{c}} = C_{\mathrm{i}} - A/g_{\mathrm{mes}}^{\mathrm{CO_2}} \quad (15)$$

in which C_{c} and C_{i} are the $\mathrm{CO_2}$ partial pressure (with the unit of pascals) inside leaf chloroplasts and that at the intercellular air space; A is the net carbon assimilation rate (with the unit of micromoles per square metre per second).

The authors of ref. 21 gave a relationship to estimate the true photosynthetic parameters (that is, the g_{mes}-including parameters) from the CLM-modelled g_{mes}-lacking parameters once $g_{\mathrm{mes}}^{\mathrm{CO_2}}$ is known:

$$y = w \times \exp\left(p\frac{w^{u}}{(g_{\mathrm{mes}}^{\mathrm{CO_2}})^{q} + v}\right) \quad (16)$$

in which y denotes parameters for a g_{mes}-explicit representation (including V_{cmax} and J_{max} at a reference temperature of 25 °C) and w denotes their counterparts in a g_{mes}-implicit representation; p, q, u and v are empirical constants: they are 0.034, 1.1253, 0.8787 and 0.4801 for V_{cmax} and 0.2935, 1.4838, 0.0858 and 0.1726 for J_{max}.

OCS soil flux. We used a mechanistic model[55] to simulate the soil flux of OCS ($F_{\mathrm{ocs\_soil}}$). This model described the OCS uptake or production together with the OCS diffusion, respectively, for each soil column of a uniform temperature, soil moisture and porosity. The Ogée soil model has been used to infer reaction rate parameters across a range of biomes and land cover types in several laboratory studies[56,57]. It has also been applied to SiB4, showing a good performance[25].

The Ogée soil model simplifies the soil OCS flux ($F_{\mathrm{ocs\_soil}}$) as:

$$F_{\mathrm{ocs\_soil}} = \sqrt{kB\theta D}\left(\mathrm{OCS_{s\_a}} - \frac{z_1^2 P}{D}\left(1 - \exp\left(\frac{-z_{\mathrm{p}}}{z_1}\right)\right)\right) \quad (17)$$

in which k is the first-order rate constant for CA-mediated OCS hydrolysis (with the unit of per second); B is the non-dimensional solubility of OCS in water (with the unit of moles per cubic metre of $\mathrm{H_2O}$/moles per cubic metre of air); θ is the volumetric soil water content (with the unit of cubic metres per cubic metre); D is the soil OCS diffusivity (with the unit of cubic metres of air per cubic metre of soil per second); $OCS_{\mathrm{s\_a}}$ is the OCS mole fraction at the soil–air interface, assumed to be identical to the OCS mole fraction at the canopy air space; z_1 is $D/(kB\theta)$; P is the OCS production rate (with the unit of moles per cubic metre per second); and z_{p} is the soil depth (=1.0 m). Various functions in equation (17) are modelled as follows.

The rate constant k in equation (17) is given by:

$$k = f_{\mathrm{CA}} \times k_{\mathrm{uncat}} \times \frac{x_{\mathrm{CA}}(T)}{x_{\mathrm{CA}}(T_{\mathrm{ref}})} \quad (18)$$

in which f_{CA} is the CA enhancement factor (see Supplementary Table 4 for its values across different PFTs); k_{uncat} is the uncatalysed reaction rate; $x_{\mathrm{CA}}(T)$ and $x_{\mathrm{CA}}(T_{\mathrm{ref}})$ are temperature response functions. The uncatalysed reaction rate k_{uncat} depends mostly on the temperature T and pH (assumed to be constant at 4.5):

$$k_{\mathrm{uncat}} = 2.15 \times 10^{-5}\left(-10{,}450\left(\frac{1}{T} - \frac{1}{T_{\mathrm{ref}}}\right)\right) + 12.7 \times 10^{-\mathrm{p}K_{\mathrm{w}} + \mathrm{pH}} \exp\left(-6{,}040\left(\frac{1}{T} - \frac{1}{T_{\mathrm{ref}}}\right)\right) \quad (19)$$

in which $\mathrm{p}K_{\mathrm{w}}$ is the dissociation constant of water (that is, 14.0). For agricultural patches, the k_{uncat} value was designated as 1/5 of the value calculated from equation (19) as agricultural soil was reported to have a lower k_{uncat} (ref. 58).

The temperature response function $x_{\mathrm{CA}}(T)$ in equation (18) is given by:

$$x_{\mathrm{CA}}(T) = \frac{\exp(-\Delta H_{\mathrm{a}}/RT)}{1 + \exp(-\Delta H_{\mathrm{d}}/RT + \Delta S_{\mathrm{d}}/R)} \quad (20)$$

in which ΔH_{a}, ΔH_{d} and ΔS_{d} are thermodynamic parameters with values of 40 kJ mol^{-1}, 200 kJ mol^{-1} and 660 J mol^{-1} K^{-1}, respectively

The non-dimensional solubility B of OCS in water in equation (17) is related to Henry's law constant K_{H} (with the unit of moles per square metre per pascal) and depends on temperature:

$$B = k_{\mathrm{H}} \times R \times T;\ k_{\mathrm{H}} = 2.1 \times 10^{-4} \times \exp\left(\frac{24{,}900\left(\frac{1}{T} - \frac{1}{298.15}\right)}{R}\right) \quad (21)$$

The soil OCS diffusivity D in equation (17) is calculated as[25]:

$$D = D_{\mathrm{eff,a}} + D_{\mathrm{eff,l}} \times B;\ D_{\mathrm{eff,a}} = D_{0,\mathrm{a}}(T) \times \tau_{\mathrm{a}} \times \varepsilon_{\mathrm{a}};\ D_{\mathrm{eff,l}} = D_{0,\mathrm{l}} \times \tau_{\mathrm{l}} \times \theta \quad (22)$$

in which $D_{\mathrm{eff,a}}$ and $D_{\mathrm{eff,l}}$ are the effective diffusivities of gaseous OCS and dissolved OCS through the soil matrix, respectively; $D_{0,\mathrm{a}}$ refers to the binary diffusivity relative to temperature as: $D_{0,\mathrm{a}}(T) = D_{0,\mathrm{a}}(298.15\ \mathrm{K})(T/298.15\ \mathrm{K})^{1.5}$, in which $D_{0,\mathrm{a}}(298.15\ \mathrm{K})$ (or $D_{0,\mathrm{a}}(25\ ^{\circ}\mathrm{C})$) equals $1.27 \times 10^{-5}\ \mathrm{m^2\ s^{-1}}$; $D_{0,\mathrm{l}}$ is also relative to temperature: $D_{0,\mathrm{l}}(T) = D_{0,\mathrm{l}}(T_0)(T/T_0 - 1)^{1.5}$, in which T_0 is 216 K (−57.15 °C) and $D_{0,\mathrm{l}}(T_0)$ can be calculated as $D_{0,\mathrm{l}}(298.15\ \mathrm{K})/(298.15\ \mathrm{K}/T_0 - 1)^{1.5}$ with $D_{0,\mathrm{l}}(298.15\ \mathrm{K})$ equal to $1.94 \times 10^{-9}\ \mathrm{m^2\ s^{-1}}$; τ_{a} and τ_{l} are the tortuosity factors used to describe the tortuous movement through the air- or water-filled pore space. We selected the τ_{a} function[59] formed as $(0.2(\varepsilon_{\mathrm{a}}/\phi)^2 + 0.004)/\phi$, in which ε_{a} is the volumetric air content and ϕ is the total soil porosity, and τ_{l} function[60] formed as $\theta^{7/3}/\phi^2$, in which θ is the volumetric water content as they are independent of pore-size distribution[25].

The OCS production rate P in equation (17) is assumed to be uniform from the surface to depth z_{p} (= 1.0 m) and controlled by soil temperature T_{soil} (in degrees Celsius):

$$P = j \times \exp(m \times T_{\mathrm{soil}}) \quad (23)$$

in which j and m are empirical parameters whose average values across different PFTs are given in Supplementary Table 4.

Inference of GPP from plant OCS fluxes

OCS plant uptake is used to infer GPP, once the concentration-normalized ratio of OCS and CO_2 uptake (LRU) is known:

$$\mathrm{GPP} = F_{\mathrm{ocs\_veg}} \frac{[\mathrm{CO_2}]_{\mathrm{a}}}{[\mathrm{OCS}]_{\mathrm{a}}} \frac{1}{\mathrm{LRU}} \quad (24)$$

in which $[CO_2]_a$ denotes the ambient concentration of CO_2. For inferring GPP from site-level simulations, site measurements of $[CO_2]_a$ and $[OCS]_a$ were used herein; whereas for inferring GPP at the global scale, model simulations of $[CO_2]_a$ and $[OCS]_a$ were used.

LRU has been estimated in some experimental studies[17]. Measurements carried out in 22 C_3 plant species reported cross-species ranges of LRU with a mean value of 1.61 (±0.26)[39], which has been adopted by previous studies in evaluating GPP–OCS relationships at sites or globally[14,61]. However, a constant LRU cannot accurately translate plant OCS uptake to GPP, as LRU was observed to decrease with increasing PAR at both the leaf and ecosystem scales[38,51]. Here we applied two approaches to calculating the LRU for C_3 species (a constant LRU of 1.16 was used for C_4 species for both approaches, as C_4 species were reported to have a much lower LRU[29,61]) and obtained two estimates of OCS-inferred GPP from equation (24). First, a constant LRU value of 1.61 was adopted, leading to a GPP estimate termed as $\mathrm{GPP_{OCS\_LRU\_constant}}$. Second, we considered the LRU variations in response to light intensity, and adopted the empirical equation between LRU and PAR proposed previously[38] at FI-Hyy (equation (25)). The applicability of the LRU–PAR relationship in estimating GPP (the resulting GPP is termed as $\mathrm{GPP_{OCS\_LRU\_PAR}}$) was evaluated at two sites in different biomes (Fig. 3 and Supplementary Fig. 10). The two OCS-inferred GPPs were compared with each other and also with that directly simulated by the CLM5 with the default FvCB model (termed $\mathrm{GPP_{CLM5\_FvCB}}$; Supplementary Table 5).

$$\mathrm{LRU} = 607.2623/\mathrm{PAR} + 0.5705 \quad (25)$$

Comparison of OCS-inferred GPP with in situ canopy-scale GPP in Amazon rainforests

Both OCS-inferred and CLM5 FvCB-simulated GPP were compared with in situ GPP partitioned from in situ NEE measurements at four tropical sites located in the central and eastern Amazon. Here the GPP dataset came from the Large-Scale Biosphere-Atmosphere Experiment in the Amazon Ecology dataset[62], which has been harmonized across projects with additional quality control checks carried out, and aggregated to several time intervals. The four sites were selected (following ref. 48) because: they represent mature intact tropical forests in the Amazon that are highly productive, and they span a range of dry-season intensities and lengths. The simulation design and model–data comparison at these four sites are provided in Supplementary Text 6.

Monte Carlo simulations of uncertainties in GPP estimates arising from cross-PFT variabilities in LRU and its light dependency

GPP uncertainty may arise from cross-species or PFT variabilities in LRU and its light dependency. To systematically assess this uncertainty, we combined best available field measurements with Monte Carlo simulations to generate ensemble estimates of GPP based on diverse combinations of PFT-specific LRU–PAR relationships. The core of this approach is to construct diverse combinations of PFT-specific LRU–PAR relationships guided by field measurements. To achieve this, we generated ensemble LRU–PAR relationships by randomly sampling data points from two types of field dataset to mimic cross-species variability (Supplementary Text 5). The two field datasets used here are: leaf-level measurements of ref. 38, so far the only publicly available leaf-scale dataset with paired LRU–PAR along a full range of PAR continuum and with concurrent canopy-level OCS flux measurements that can facilitate scaling from leaf to canopy scales; and datasets compiled in ref. 39, so far the only dataset available that has LRU measurements under multiple standardized PAR levels across diverse PFTs and species. Reference 38 provided continuous and paired LRU–PAR measurements in the full PAR range. It offers the baseline 'shape' (functional relationship) between LRU and PAR that all plant species may follow (that is, a linear relationship between LRU and 1/PAR; or a hyperbolic relationship between LRU and PAR). Then we applied the cross-PFT variability by varying the slopes and intercepts of the baseline linear shapes. This was achieved by imposing random variations (representing cross-species variability) to the 'baseline' shape, with the random variation generated from the dataset of ref. 39. We chose measurements from ref. 39 (synthesized in its Table II) to represent species variability in LRU and its PAR dependency, primarily because: it covered LRUs from 22 species in total belonging to 4 different biome types; it provided LRU values for each species at 3 different (and standardized) light levels (that is, 179, 352 and 1,889 μmol $\mathrm{m^{-2}\ s^{-1}}$), which allowed us to quantify LRU variability arising from species differences under multiple light levels; and these LRUs were measured at the same environmental conditions including CO_2 concentration, air temperature and humidity, ensuring that the LRU variability primarily comes from PAR for each species.

Although there are other studies that synthesized LRU values across species from the literature (for example, ref. 17), these values came from different studies under diverse combinations of environmental conditions, without standardizing PAR levels or controlling other environmental factors, precluding the possibility to systematically quantify the variability of LRU–PAR dependency across species. There are also attempts to use the optimization theory to generate global mapping of LRU (for example, ref. 63), but challenges still remain with this approach in quantifying LRU–PAR relationships under unsaturated light conditions. More field measurements are needed to better characterize LRU variability with light across PFTs.

Design of CLM5 model simulations

We used the Community Earth System Model CLM5 as the TBM for OCS simulation. Four simulations were carried out, with different parameterizations of $g_{\mathrm{t}}^{\mathrm{OCS}}$ (Supplementary Table 6). For simulation 1 (g_{mes}-implicit simulation), we implemented the OCS plant model with implicit mesophyll diffusion[16]. For simulation 2 (g_{mes}-explicit simulation), the OCS plant model with explicit mesophyll diffusion was implemented,

with g_{mes} calculated by a process-based model[24]. Comparison between simulations 1 and 2 shows the impact of mechanistic consideration of mesophyll diffusion in OCS flux simulation. For simulation 3 (g_{mes}-excluding simulation), we assumed g_{mes} to be infinite (that is, ignoring mesophyll resistance) and computed g_t^{OCS} with only g_b^{OCS}, g_s^{OCS} and g_{CA}^{OCS}. Comparison between simulations 2 and 3 shows the effect of mesophyll diffusion on OCS fluxes. For simulation 4, we implemented explicit g_{mes} while using a temperature response function for g_{CA}^{OCS} (equation (10)). Comparison between simulations 2 and 4 shows the impact of g_{CA}^{OCS} parameterization on OCS simulation.

Each simulation was run with active biogeochemistry and crop models and was preceded by a spin-up for 100 years. We carried out both global simulations and point simulations. For global simulation, all scenarios from simulation 1 to simulation 4 were performed from 2000 to 2010. Meteorological data from the Global Soil Wetness Project Phase 3 National Centers for Environmental Prediction dataset on a 3-h interval (available from 1901 to 2014) were used as meteorological forcing. Point simulation was run at two field sites: FI-Hyy (2013–2017) and US-Ha1 (2012–2013), for which OCS observations exist across most months within a year[38,51] and partitioned GPP estimates were also available for growing seasons[38,64] (Supplementary Table 3). For each site, the PFT in the model simulation was set as consistent with the site land cover type, and site observations of meteorological conditions were used as meteorological forcing.

Data availability

The CLM5 simulation output related to this study is available at https://doi.org/10.7298/mxg9-7176.

52. Ma, J. et al. Inverse modelling of carbonyl sulfide: implementation, evaluation and implications for the global budget. *Atmos. Chem. Phys.* **21**, 3507–3529 (2021).
53. Badger, M. R. & Price, G. D. The role of carbonic anhydrase in photosynthesis. *Annu. Rev. Plant Biol.* **45**, 369–392 (1994).
54. Evans, J. R., Caemmerer, S. V., Setchell, B. A. & Hudson, G. S. The relationship between CO_2 transfer conductance and leaf anatomy in transgenic tobacco with a reduced content of Rubisco. *Funct. Plant Biol.* **21**, 475–495 (1994).
55. Ogée, J. et al. A new mechanistic framework to predict OCS fluxes from soils. *Biogeosciences* **13**, 2221–2240 (2016).
56. Meredith, L. K. et al. Coupled biological and abiotic mechanisms driving carbonyl sulfide production in soils. *Soil Systems* **2**, 37 (2018).
57. Meredith, L. K. et al. Soil exchange rates of COS and $CO^{18}O$ differ with the diversity of microbial communities and their carbonic anhydrase enzymes. *ISME J.* **13**, 290–300 (2019).
58. Kaisermann, A., Jones, S. P., Wohl, S., Ogée, J. & Wingate, L. Nitrogen fertilization reduces the capacity of soils to take up atmospheric carbonyl sulphide. *Soil Systems* **2**, 62 (2018).
59. Deepagoda, T. K. K. C. et al. Density-corrected models for gas diffusivity and air permeability in unsaturated soil. *Vadose Zone J.* **10**, 226–238 (2011).
60. Millington, R. J. & Quirk, J. P. Permeability of porous solids. *Trans. Faraday Soc.* **57**, 1200–1207 (1961).
61. Asaf, D. et al. Ecosystem photosynthesis inferred from measurements of carbonyl sulphide flux. *Nat. Geosci.* **6**, 186–190 (2013).
62. Restrepo-Coupe, N. et al. LBA-ECO CD-32 flux tower network data compilation, Brazilian Amazon: 1999–2006, V2. ORNL DAAC (2021).
63. Wohlfahrt, G., Hammerle, A., Spielmann, F., Kitz, F. & Yi, C. Technical note: Novel estimates of the leaf relative uptake rate of carbonyl sulfide from optimality theory. *Biogeosciences* **20**, 589–596 (2023).
64. Wehr, R. et al. Seasonality of temperate forest photosynthesis and daytime respiration. *Nature* **534**, 680–683 (2016).

Acknowledgements J.L. acknowledges the Saltonstall Fellowship and Barbara McClintock Award from the School of Integrative Plant Science at Cornell University. Y.S. acknowledges funding from the National Science Foundation (NSF) Macrosystem Biology (award 1926488). D.L. acknowledges funding from the NSF (number 2039932). Part of this work was carried out at the Jet Propulsion Laboratory, California Institute of Technology, under a contract with the National Aeronautics and Space Administration (80NM0018D0004). L.K. was supported by NASA (the National Aeronautics and Space Administration), USA (ECOSTRESS Science and Applications Team: grant number 80NSSC20K0215). L.G. acknowledges support from the US Department of Energy (DOE), Office of Science, Biological and Environmental Research Program. The funding for L.G. was through the Oak Ridge National Laboratory Terrestrial Ecosystem Sciences Science Focus Area. This manuscript has been co-authored by UT-Battelle under contract number DE-AC05-00OR22725 with the US DOE. This work is supported by the NSF National Center for Atmospheric Research (NCAR), which is a major facility sponsored by the NSF under Cooperative Agreement number 1852977. Specifically, we acknowledge the computing resources made available to Y.S. and J.L., including the Cheyenne and Derecho supercomputers provided by the Computational and Information Systems Laboratory (CISL) at the NCAR. Y.S., L.K. and J.E.C. acknowledge the 2017 Keck Institute for Space Studies workshop 'Next-Generation Approach for Detecting Climate-Carbon Feedbacks: Space-Based Integration of Carbonyl Sulfide (OCS), CO_2, and Solar Induced Fluorescence (SIF)'. The US government retains — and the publisher, by accepting the article for publication acknowledges that the US government retains — a non-exclusive, paid-up, irrevocable, world-wide license to publish or reproduce the published form of this work, or allow others to do so, for US government purposes. The US DOE will provide public access to these results of federally sponsored research in accordance with the DOE Public Access Plan (http://energy.gov/downloads/doe-public-access-plan).

Author contributions Y.S. and J.L. conceived of the study. J.L. and Y.S. developed the methodology. J.L. conducted the analyses. J.L. and Y.S. interpreted the results; L.M.J.K., W.S., D.L., J.E.C., L.G., Y.L. and L.K. helped with the interpretation. J.L. and Y.S. constructed the initial draft, and L.M.J.K., W.S., D.L., J.E.C., L.G., Y.L. and L.K. contributed critically to the subsequent revision of manuscript.

Competing interests The authors declare no competing interests.

Additional information
Supplementary information The online version contains supplementary material available at https://doi.org/10.1038/s41586-024-08050-3.

Correspondence and requests for materials should be addressed to Ying Sun.

Peer review information *Nature* thanks Teresa Gimeno and the other, anonymous, reviewer(s) for their contribution to the peer review of this work.